The Role of Whitecapping in Thickening the Ocean Surface Boundary Layer

GREGORY P. GERBI AND SAMUEL E. KASTNER

Skidmore College, Saratoga Springs, New York

GENEVIEVE BRETT

Massachusetts Institute of Technology/Woods Hole Oceanographic Institution Joint Program, Cambridge, Massachusetts

(Manuscript received 24 November 2014, in final form 13 May 2015)

ABSTRACT

The effects of wind-driven whitecapping on the evolution of the ocean surface boundary layer are examined using an idealized one-dimensional Reynolds-averaged Navier–Stokes numerical model. Whitecapping is parameterized as a flux of turbulent kinetic energy through the sea surface and through an adjustment of the turbulent length scale. Simulations begin with a two-layer configuration and use a wind that ramps to a steady stress. This study finds that the boundary layer begins to thicken sooner in simulations with whitecapping than without because whitecapping introduces energy to the base of the boundary layer sooner than shear production does. Even in the presence of whitecapping, shear production becomes important for several hours, but then inertial oscillations cause shear production and whitecapping to alternate as the dominant energy sources for mixing. Details of these results are sensitive to initial and forcing conditions, particularly to the turbulent length scale imposed by breaking waves and the transfer velocity of energy from waves to turbulence. After 1–2 days of steady wind, the boundary layer in whitecapping simulations has thickened more than the boundary layer in simulations without whitecapping by about 10%–50%, depending on the forcing and initial conditions.

1. Introduction

Turbulent mixing in the ocean surface boundary layer is a process that influences stratification, vertical structure of currents and plankton, and air sea exchange of gases and heat. Classic work assumed that ocean surface turbulence is generated by the same processes as one would expect at a rigid boundary. In stable buoyancy conditions, this means that shear production is the energy source for turbulence, extracting energy from the mean flow and transforming it into turbulent kinetic energy. Idealized and analytical models for boundary layer thickness have a long history of use for predicting boundary layer thickness under assumptions of rigid boundary turbulence (e.g., Price et al. 1986; Trowbridge 1992). More recently, surface gravity waves have been recognized as an energy source for turbulence via Langmuir turbulence (Craik and Leibovich 1976; McWilliams et al. 1997; Teixeira 2012) and wind-driven whitecapping (Agrawal et al. 1992; Gemmrich et al. 1994; Craig and Banner 1994; Terray et al. 1996; Drennan et al. 1996). Recent research has focused on understanding the dynamics and effects of these wave-driven processes (Gerbi et al. 2009; Kukulka et al. 2010; D'Asaro 2014; Thomson et al. 2014).

The work presented here focuses on the effects of whitecapping on boundary layer thickness and structure. Including whitecapping effects in numerical models affects the trajectories of surface drifters (Carniel et al. 2009), sea surface temperature (Zhang et al. 2011), and the behavior of buoyant coastal plumes (Gerbi et al. 2013); observations show that whitecapping is likely to affect boundary layer structure in buoyant plumes (Thomson et al. 2014). This work does not address Langmuir turbulence, which continues to be an active research area explored through observations, numerical models, and analytical models (e.g., Gemmrich 2012; Kukulka et al. 2012; Sullivan et al. 2012; Teixeira 2012; D'Asaro et al. 2014; McWilliams et al. 2014; Harcourt

Corresponding author address: Gregory P. Gerbi, Physics and Geosciences Departments, Skidmore College, 815 North Broadway, Saratoga Springs, NY 12866.
E-mail: ggerbi@skidmore.edu

DOI: 10.1175/JPO-D-14-0234.1

2015). Whitecapping can be a larger source of turbulent kinetic energy than the Stokes shear instabilities that produce Langmuir turbulence (Gerbi et al. 2009) and has its strongest effects in the upper several meters of the ocean. However, Langmuir turbulence has been shown to both cause vertical transport of water with high dissipation rates of turbulent kinetic energy (Thorpe et al. 2003) and to concentrate bubbles whose buoyancy acts to reduce turbulent kinetic energy (Gemmrich 2012). These somewhat conflicting observations suggest that the interaction between whitecapping and Langmuir turbulence is complicated.

As winds cause surface gravity waves to grow, those waves break intermittently. This whitecapping transfers energy from the wave field into turbulent kinetic energy (TKE) (Gemmrich et al. 1994; Terray et al. 1996). The injection itself is complicated and not fully understood (Gemmrich 2010), but at depths deeper than the wave troughs, the TKE is transported downward by turbulence, and a balance between flux divergence and dissipation of turbulent kinetic energy has been suggested by observations (Gemmrich et al. 1994; Terray et al. 1996; Thomson et al. 2013) and large-eddy simulations (Sullivan et al. 2004, 2007). Most of the detailed research studying relationships between wind-driven whitecapping and turbulence dynamics has been in relatively unstratified waters, and it often examines only the steady-state, fully developed boundary layer (e.g., Gemmrich et al. 1994; Terray et al. 1996; Sullivan et al. 2007; Gerbi et al. 2009; McWilliams et al. 2012). Recent work has begun to focus on time-dependent processes in stratified and horizontally inhomogeneous waters. Vagle et al. (2012) examined variations of dissipation rate above trough level and found that turbulence was suppressed when surface heat flux was strong. Thomson et al. (2014) studied whitecapping driven by convergent surface currents and found evidence suggesting that whitecapping could enhance turbulent mixing at the base of a buoyant river plume.

The work described in this paper was undertaken in an attempt to determine the importance of whitecapping on boundary layer evolution and to understand some of the findings of Gerbi et al. (2013) and Burchard (2001) in more detail. Gerbi et al. (2013) examined the evolution of a buoyant coastal current as it propagated offshore under steady upwelling-favorable winds in an idealized numerical model. That work found that the simulations with whitecapping had a thicker freshwater plume than simulations without whitecapping. However, the majority of the thickness difference was explained by differences in evolution during the first day of winds, and later the evolution of the plume thickness was complicated and not related to the presence of whitecapping in a simple way. Burchard (2001) examined an offshore environment by comparing observational profiles during and after a storm in the North Sea with one-dimensional numerical models. He found that although the vertical structure was affected by whitecapping, the boundary layer thickness of 10–20 m was largely similar whether or not whitecapping was included in the turbulence parameterization. These studies, among others, led us to ask under what conditions does whitecapping play a role in thickening the surface boundary layer and how large is that role.

In this paper, we use a one-dimensional Reynolds-averaged Navier–Stokes numerical model to study the energetics of thickening a surface boundary layer whose initial configuration is a thin layer of light water overlying a thick layer of denser water. We attempt to put our results in the context of previous work on boundary layer thickening by Trowbridge (1992), who developed an analytical theory for boundary layer thickening in nonrotating systems. In sections 2 and 3, we describe the numerical model, numerical experiments, and the results of those experiments. In section 4, we examine the dynamics of boundary layer thickening in the presence and absence of wind-driven whitecapping, including looking at some of the transient properties of boundary layer thickening as the wind and inertial oscillations evolve.

2. Methods

a. Overview

This study uses a one-dimensional configuration of the Regional Ocean Modeling System (ROMS; http://www.myroms.org). ROMS is a hydrostatic primitive equation model, and its computational kernel has been described by Shchepetkin and McWilliams (2005, 2008) and Haidvogel et al. (2008) [as corrected by Shchepetkin and McWilliams (2009)]. We configure ROMS to behave as a one-dimensional model by using six grid cells with periodic boundary conditions in each horizontal dimension. Water depth is set to 100 m with 1000 vertical layers of uniform thickness, and the time step is 30 s. No heat or salt flux is allowed through the sea surface. We use no tidal forcing, and the surface momentum forcing is applied through a surface wind stress. Wind stress is ramped sinusoidally from zero to one of three values over the first 4 h of simulation and is held constant at that value for the remainder of the simulation (Fig. 1). Temperature is vertically uniform and constant in all simulations. Initial conditions are a quiescent two-layer fluid, with a thin upper layer overlying a thick lower layer. Each layer has constant salinity. The initial upper-layer

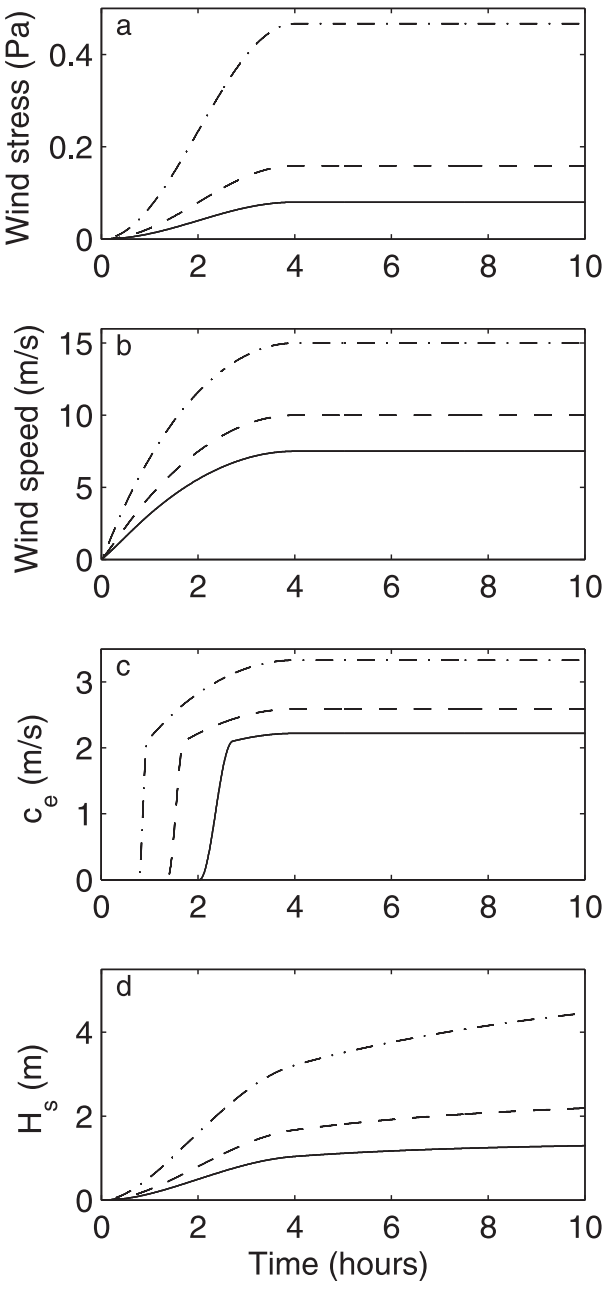

FIG. 1. Forcing used in these simulations as functions of time. (a) Wind stress. (b) Wind speed. (c) Effective energy transfer coefficient. (d) Significant wave height. The solid, dashed, and dashed–dotted lines correspond to the conditions under the three different wind stress regimes in the simulations. The maximum stresses are equivalent to wind speeds of 7.5, 10, and 15 m s^{-1}, respectively. Waves continue to grow past hour 10 until they reach heights of 1.4, 2.4, and 5.5 m, as specified by (6) and (8).

thickness and salinity vary between simulations; the lower layer extends to the base of the 100-m water column. Details of forcing and initial conditions in the simulations are given in section 2c.

We use the k–ε two-equation turbulence closure model for all turbulence dynamics (Jones and Launder 1972; Burchard and Baumert 1995; Warner et al. 2005), and we vary the presence or absence of parameterizations of shear production or wind-driven whitecapping, which is discussed further in section 2b. In the k–ε model, TKE evolves according to

$$\frac{dk}{dt} = \mathrm{SP} + \mathrm{BP} - \frac{dF}{dz} - \varepsilon, \tag{1}$$

where k is the TKE; t is the time; SP is the shear production that extracts energy from the mean flow; BP is buoyancy production, which adds or subtracts energy from the density field; F is the vertical flux of TKE by turbulence (F is negative for downward flux); z is the vertical coordinate, positive upward, with $z = 0$ at the sea surface; and ε is the dissipation rate. Divergence of flux of TKE dF/dz is parameterized in the k–ε model with a turbulent diffusivity. Buoyancy production is generally positive in gravitationally unstable conditions and negative in stable stratification. In many situations, dk/dt is small compared to other terms in (1) (Gerbi et al. 2009; Scully et al. 2011).

b. Whitecapping parameterization

Whitecapping is parameterized using a modified version of the method of Craig and Banner (1994) and Burchard (2001), first implemented in ROMS by Carniel et al. (2009). This method represents breaking waves by adding a downward flux of TKE through the sea surface and changing the turbulent length scale at the sea surface (Terray et al. 1996; Jones and Monismith 2008b). This parameterization simplifies the wave field, needing only the significant wave height to determine a surface mixing length. It also simplifies the dynamics immediately below the sea surface, ignoring the details of the velocity field beneath breaking waves that have been examined by Gemmrich (2010, 2012). The parameterization has been successfully used to explain observations of TKE and the dissipation rate of TKE at depths below the wave troughs (Terray et al. 1996; Feddersen et al. 2007; Jones and Monismith 2008a; Gerbi et al. 2009).

Following Gemmrich et al. (1994), Terray et al. (1996), and Hwang (2009), the TKE flux through the sea surface due to whitecapping F_0 is approximated as

$$F_0 = -c_e \frac{\tau}{\rho_0} = -c_e u_*^2, \tag{2}$$

where τ is the wind stress; ρ_0 is a representative water density; $u_* = \sqrt{\tau/\rho_0}$ is the friction velocity of the water; and c_e is an effective energy transfer velocity that characterizes the rate of energy input from the wind to the waves.

Field estimates of c_e are scattered, but the relationship between wind speed and c_e is roughly linear for young waves (Hwang 2009). At wind speeds between 7 and 15 m s^{-1} Hwang finds the best fit to observations as

$$c_e = aU_{10} + b; \quad a = 0.148, \quad b = 1.11\,\mathrm{m\,s^{-1}}, \tag{3}$$

where U_{10} is the wind speed at 10 m above the mean sea surface and a and b are empirical constants. This gives values of c_e of roughly 2–3 m s^{-1}. Other studies (e.g., Gemmrich et al. 1994; Terray et al. 1996) find values of c_e that are smaller by factors of 2–5.

In this study, we compute c_e using (3), and we relate U_{10} and τ using the COARE 3.0 neutral drag coefficient described by Fairall et al. (2003):

$$\tau = \rho_{\mathrm{air}} C_{10} U_{10}^2, \tag{4}$$

where C_{10} is the drag coefficient, and ρ_{air} is the density of air. The drag coefficient varies with wind speed and is between $\sim 1.0 \times 10^{-3}$ and $\sim 1.7 \times 10^{-3}$ for the range of winds studied here. In our whitecapping parameterization, c_e (and therefore F_0) is set to zero at low wind speeds. This accounts for anecdotal and observational evidence that whitecapping is limited or absent in weak wind conditions (Munk 1947; Hwang 2009). For numerical stability, we ramp c_e from zero to the value given by (2) for u_*^2 between 4×10^{-5} and 6×10^{-5} m^2 s^{-2} (equivalent to wind speeds $\sim$5–6 m s^{-1}; Fig. 1).

Changes in the sizes of turbulent eddies are represented in the whitecapping parameterization by changes in the turbulent length scale. In particular, this allows larger eddies close to the sea surface. Previous studies have found that this mixing length is roughly 0.5–0.6 times the significant wave height of the wind waves (Terray et al. 1996; Burchard 2001; Soloviev and Lukas 2003), although Drennan et al. (1996) found that the mixing length could also be scaled by the length of the dominant wind waves. Carniel et al. (2009) and Gerbi et al. (2013) made the mixing length proportional to τ, which is equivalent to assuming full development of the wave field at all times. In the work presented here, we use an analytical approach to compute significant wave heights H_s from the wind speed, and we then compute the mixing length z_0 as

$$z_0 = c_z H_s, \tag{5}$$

where c_z is a constant that we set equal to 0.5 or 0.25 (to test the effects of a small mixing length).

To determine H_s, we follow Holthuijsen (2007), who uses the results of Pierson and Moskowitz (1964), Young and Verhagen (1996), and Breugem and Holthuijsen (2007) to give significant wave heights and peak wave periods T_p under a steady wind as

$$H_s = H_\infty [\tanh(k_1 \tilde{L}^{m_1})]^p, \quad \text{and} \tag{6}$$

$$T_p = T_\infty [\tanh(k_2 \tilde{L}^{m_2})]^q, \tag{7}$$

where $k_1 = 4.41 \times 10^{-4}$, $m_1 = 0.79$, $p = 0.572$, $k_2 = 2.77 \times 10^{-7}$, $m_2 = 1.45$, and $q = 0.187$ are empirical constants, and $\tilde{L}$ is the nondimensional fetch. Significant wave height and peak period at infinite fetch have been determined empirically by those authors as

$$H_\infty = 0.24 \frac{U_{10}^2}{g}, \quad \text{and} \tag{8}$$

$$T_\infty = 7.69 \frac{U_{10}}{g}, \tag{9}$$

where g is the acceleration due to gravity. The nondimensional fetch is

$$\tilde{L} = L_{\mathrm{eq}} \frac{g}{U_{10}^2}, \tag{10}$$

where L_{eq} is the equivalent fetch and is a function of time t. We determine the equivalent fetch using a constant group velocity c_g and the simplified relationship

$$L_{\mathrm{eq}}(t) = c_g t. \tag{11}$$

The group velocity that we use is given by the deep-water dispersion relation and the peak period for fully developed waves that are in equilibrium with the steady wind stress in the latter part of each simulation.

Although the wind stress ramps to its steady value in only 4 h, the wave heights take several to tens of hours to approach their fully developed limits (Fig. 1). Because of the smaller wind speeds during the first 4 h, this approach overestimates the equivalent fetch and allows the waves to reach their equilibrium heights a few hours sooner than they would if a dynamical wave model were used. We assess some of the effects of the resulting too long length scale by varying c_z in setting the surface mixing length using (5).

c. *Details of simulations*

We ran simulations under conditions that varied initial upper-layer thickness, initial upper-layer salinity, wind stress, and the relationships between wind stress and both mixing length and energy transfer velocity. We present results from 42 simulations, and we refer to several other simulations that we examined in order to assess sensitivity of the results to the choices of parameters, forcing, and initial conditions. In all cases the

TABLE 1. Summary of simulation physics.

Case	Shear production	Whitecapping	Rotation
SN	Yes	No	No
SWN	Yes	Yes	No
WN	No	Yes	No
S	Yes	No	Yes
SW	Yes	Yes	Yes
W	No	Yes	Yes

temperature is held constant at 15°C and the lower-layer salinity is 32. We used initial upper-layer salinities of 28, 30, and 31 and initial upper-layer thicknesses of 3 and 6 m. Wind stresses reach their steady values after 4 h in all cases. Those steady values are 0.08, 0.16, and 0.47 Pa, equivalent to wind speeds of 7.5, 10, and 15 m s^{-1} (Fig. 1). Significant heights of fully developed waves computed using (6) are 1.4, 2.4, and 5.5 m. For most simulations, we set the surface mixing length to be one-half of the significant wave height ($c_z = 0.5$), but we ran some simulations with a shorter mixing length, using $c_z = 0.25$. We also ran a small number of simulations using c_e reduced by a factor of 2 from the value given by (3). In simulations that include rotation, the Coriolis frequency is 9.1×10^{-5} s^{-1}, giving an inertial period of 19.1 h.

Our detailed analysis focuses on results from a family of simulations with one set of forcing and initial conditions. These reference conditions have maximum $\tau = 0.16$ Pa, maximum $z_0 = 1.2$ m ($H_s = 2.4$ m), $h_0 = 3$ m, and $S_1 = 30$, where h_0 is the initial thickness of the upper layer and S_1 is the initial salinity of the upper layer. The results from these reference simulations are representative of the range of conditions that we examined, and where appropriate we discuss differences between simulations in different conditions.

For each set of forcing and initial conditions, the simulations fall into six qualitative categories with different physical configurations: three without rotation (Coriolis) and three with rotation. In each of those groups, we ran simulations with shear production and no whitecapping, with whitecapping and no shear production, and with both shear production and whitecapping. The simulations with no shear production are not physically reasonable but allow us to diagnose some of the important effects of both shear production and whitecapping on boundary layer evolution. When discussing the results, we refer to the simulations, defined in Table 1, as cases SN, SWN, and WN (nonrotating) and S, SW, and W (rotating). These designations describe the model physics. Each case is examined at a range of forcing and initial conditions that are specified where appropriate in the text.

d. Analysis

For convenience, similar to Trowbridge (1992), we define the vertically integrated buoyancy anomaly B as

$$B = \int_{-H}^{0} dz \frac{g}{\rho_2}[\rho_2 - \rho(z)], \tag{12}$$

where $z = -H$ is the base of the simulation, $\rho(z)$ is the surface-referenced potential density, and ρ_2 is the potential density of the lower layer. For the two-layer initial conditions (and assuming linearity of the equation of state over the range of salinities), $\rho(z)$ is either ρ_1 (the initial potential density of the upper layer) or ρ_2, and (12) reduces to

$$B = g h_0 \frac{\rho_2 - \rho_1}{\rho_2}. \tag{13}$$

For the initial two-layer geometry, B remains constant throughout the simulation.

All calculations were made using ROMS history files, which are snapshots of the model state. We saved model output every 5 min. At each time step, boundary layer thickness was estimated as the depth of the mean salinity in the domain, which varied between 31.76 and 31.97. These values consistently lie just above the undisturbed lower layer. In simulations with small buoyancy anomaly and after the boundary layer has thickened past ~40 m, small changes in this definition can lead to several meters difference in estimates of the boundary layer thickness. Terms in the turbulent kinetic energy balance that are not output from ROMS (shear production, buoyancy production, and TKE flux divergence) were computed using turbulent viscosity or diffusivity and vertical profiles of the relevant quantities (velocity, density, and TKE).

3. Results

a. Boundary layer thickness

The presence or absence of both whitecapping and shear production of TKE affects boundary layer thickness and evolution. In all simulations, the boundary layer begins to thicken about 1–3 h after the start of the simulation—after the mean velocity and turbulence fields have evolved from their initially quiescent states (Figs. 2, 3). The boundary layer thickens earlier in simulations with whitecapping than it does in simulations with no whitecapping.

The presence or absence of rotation has important effects, largely related to the ability of shear production

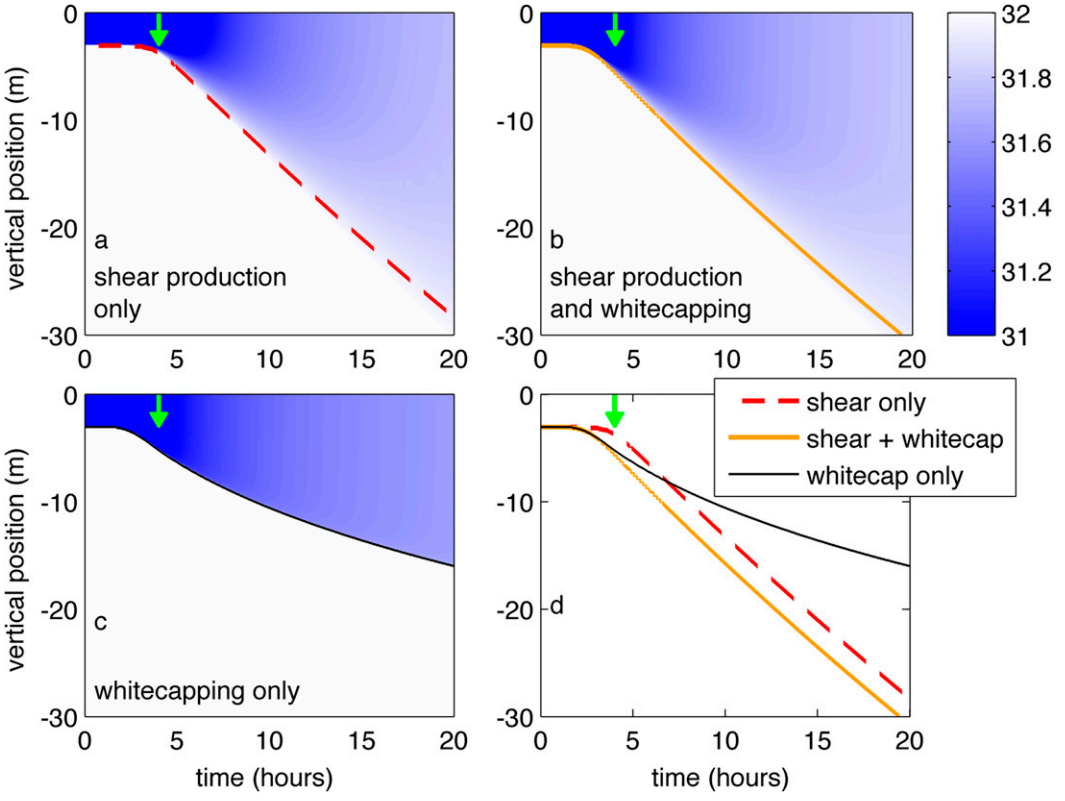

FIG. 2. Evolution of salinity in nonrotating reference frame using the reference set of forcing and initial conditions. (a) Case SN is shear production but no whitecapping. (b) Case SWN indicates shear production and whitecapping. (c) Case WN is whitecapping but no shear production. (d) Comparison of thickness of boundary layer in the three simulations. Minimum salinity in the domain is 30, so the color axis is saturated in the first few hours to make variability at the base of the boundary layer more apparent. The lines correspond to the depths of the 31.94-psu isopycnal in each simulation. Time zero is at the start of the simulation. The green vertical arrow at 4 h in each panel marks the time that the wind stress reaches its steady value. Forcing and initial conditions in these simulations are maximum wind stress $\tau = 0.16$ Pa; maximum surface mixing length $z_0 = 1.2$ m ($H_s = 2.4$ m); and initial upper-layer thickness and salinity $h_0 = 3$ m and $S_1 = 30$.

to provide energy for thickening (discussed further below). In simulations without rotation, after about 3 h, the boundary layer in cases SN and SWN thickens at the same, constant rate, which is faster than the thickening rate for case WN (Fig. 2). This occurs across the range of conditions that we examined (not shown).

In simulations with rotation, the evolution of thickening rates is more complicated. After the wind has reached its steady strength (at 4 h), all cases thicken at similar rates for the next ~6 h (Fig. 3), although case SW is consistently fastest, followed by case S and then case W. After about 10 h of simulation, inertial oscillations reduce the effect of shear production and the thickening rate in case S is periodically near zero. In case W, the thickening is identical to that in the nonrotating case WN, because the turbulence in case W is tied only to the wind stress and wave height that, in these idealized simulations, are independent of inertial oscillations. After about 15–20 h, the boundary layer in case W is thicker than that in case S for most of the conditions that we examined (Figs. 4, 5), with the exception of simulations with reduced surface mixing length. In the rotating simulations, case SW has the thickest boundary layer. Like in case S, the thickening rate in case SW varies with inertial oscillations, but the rate is generally not reduced to zero, and it is not reduced for as long during each oscillation.

Changes in initial conditions have quantitative effects on the boundary layer thickness, but the qualitative characteristics are similar across the range of conditions that we examined, including one set of simulations that had an initial boundary layer thickness of 12 m (not shown). In simulations with larger initial salinity of the upper layer (smaller buoyancy anomaly), the boundary layer thickening rates are faster than in simulations with smaller initial salinity (cf. the columns of Fig. 4). In

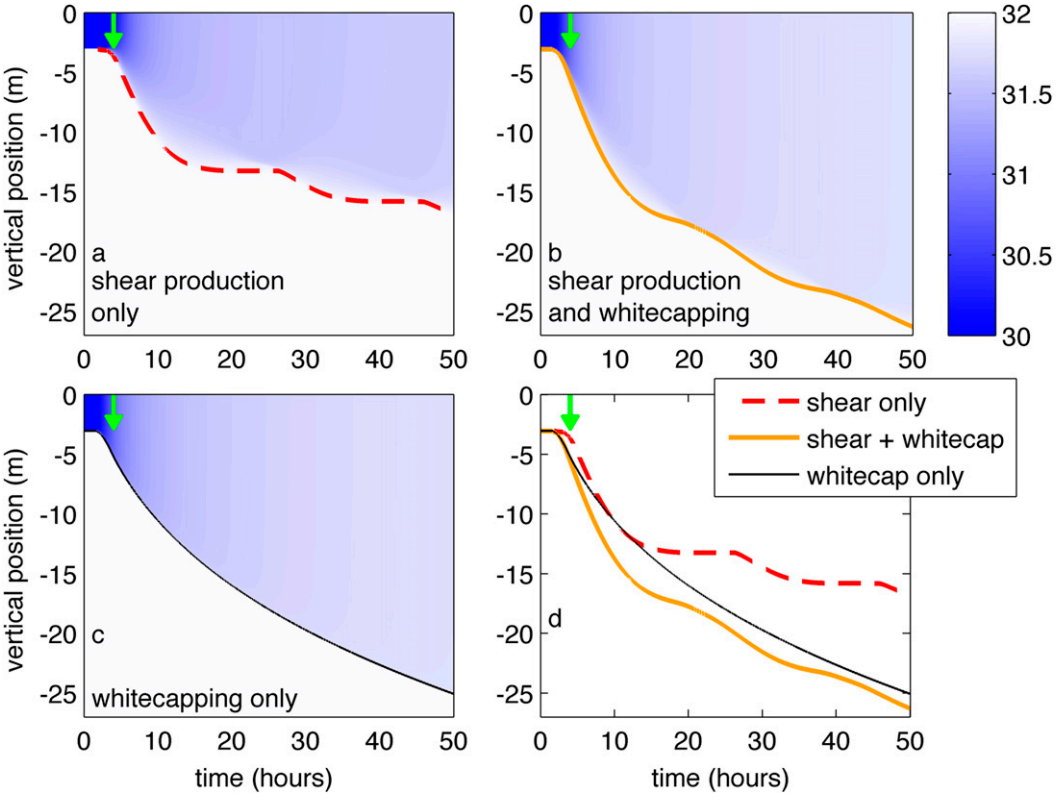

FIG. 3. As in Fig. 2, but in rotating reference frame. (a) Case S indicates shear production but no whitecapping. (b) Case SW indicates shear production and whitecapping. (c) Case W indicates whitecapping but no shear production. (d) Comparison of thickness of boundary layer in the three simulations. Horizontal axes are scaled differently than in Fig. 2.

simulations with a smaller initial thickness of the upper layer, the thickening rates are faster than in simulations with a larger initial thickness (cf. the rows of Fig. 4). Interestingly, after 10–15 h, the boundary layer is thicker in simulations with smaller h_0 than in simulations with large h_0 (for the same initial S_1). This is likely related to the vertically integrated buoyancy anomaly B. After 10–15 h in these simulations, the boundary layer evolution seems to be controlled by B rather than by h_0. For example, the simulations with $S_1 = 31$ and $h_0 = 6$ m (Fig. 4c) and $S_1 = 30$ and $h_0 = 3$ m (Fig. 4e) have nearly identical B. After the boundary layer thicknesses in Fig. 4e reach values close to those in Fig. 4c, both sets of simulations undergo similar evolution. The same can be seen in Figs. 4b and 4d, which also have nearly identical B.

Changes in wind stress (and the related changes in F_0 and z_0) have substantial effects on the boundary layer thickness (cf. columns of Fig. 5). At high wind stresses the boundary layer thickens faster, and the effect of inertial oscillations is much weaker in case SW than in low wind stress conditions. The transition at ~10 h from initially rapid thickening to slower thickening is still present in case SW at most wind stresses. For simulations with $c_z = 0.5$ and c_e given by (3), case SW is usually slightly thicker than case W, particularly at later times and high stresses. After the development of inertial oscillations, those differences are small compared to the differences between case SW and case S. This suggests that whitecapping dominates the thickening when wind is strong and shear production is limited by rotation.

The mixing length and the effective energy transfer velocity used in whitecapping cases (SW and W) have important effects on both the thickening rate and the relative importance of shear production and whitecapping as energy sources. Reducing the mixing length by a factor of 2, by setting $c_z = 0.25$, reduces the effect of whitecapping substantially (cf. the middle and bottom rows of Fig. 5). Case W thickens more slowly than case S under most conditions. Case SW still thickens more quickly than the other two cases, but its thickening rate is reduced. In addition, the effect of inertial oscillations in case SW is much stronger with smaller mixing lengths than with larger mixing lengths. This suggests that

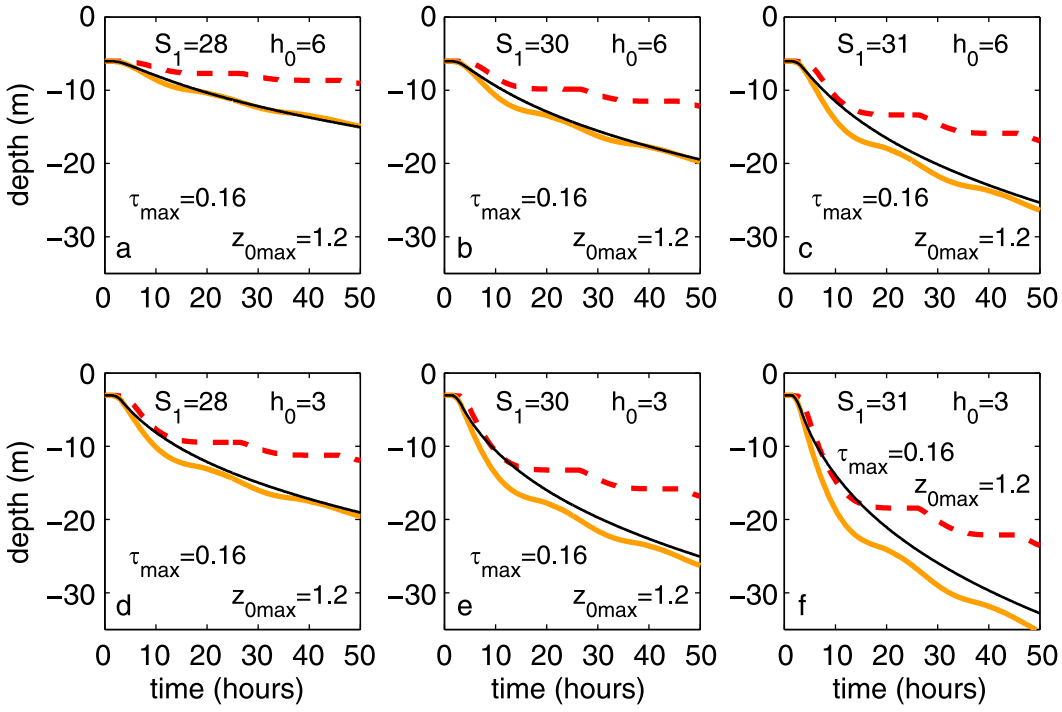

FIG. 4. Evolution of boundary layer thickness for different initial conditions. Lines show thickness in cases S, SW, and W with same line styles as in Fig. 2. Initial boundary layer thickness changes from top to bottom panels. Initial salinity changes from left to right. All have maximum wind stress, τ_{max}, of 0.16 Pa (10 m s^{-1} wind speed) and maximum mixing length, z_{0max}, of 1.2 m. Inset text gives initial upper-layer salinity, initial boundary layer thickness (m), maximum wind stress (Pa), and maximum mixing length (m) for each set of simulations. (b),(e) As in Figs. 5b and 5e. (e) shows the reference simulations, which are also shown in Fig. 3.

accurate estimates of wave heights (or other quantities that control the mixing length) are essential for studies of boundary layer mixing by whitecapping. We found similar results when, instead of changing the mixing length, we held c_z at 0.5 and reduced c_e by a factor of 2 for two different wind stresses (not shown). However, the effect of reducing the surface TKE flux was slightly smaller than the effect of reducing the mixing length.

b. *Boundary layer structure*

The vertical structures of the simulations show many similarities and several important differences. The qualitative results are similar across the range of initial and forcing conditions that we examined. We discuss cases with rotation explicitly. Nonrotating simulations have similar characteristics, with the obvious exceptions of crosswind velocities and inertial oscillations, which are not present in the nonrotating simulations.

In all the simulations the surface boundary layer has a region of somewhat uniform salinity above a region of stratified water (Figs. 6a–c). Crosswind velocity in rotating simulations is also more homogeneous in the upper part of the boundary layer than in the lower part (Figs. 6d–f). Downwind velocity shows similar vertical structure in cases SW and W, but in case S it is sheared all the way to the surface, with a slight enhancement in shear in the upper meter (Figs. 6g–i). Under all forcing and initial conditions, vertical gradients in the upper part of the boundary layer are weaker in cases with whitecapping than without. The upper part of the boundary layer is better mixed in the presence of whitecapping, which is consistent with observations (Gerbi et al. 2008; Scully et al. 2015, manuscript submitted to *J. Phys. Oceanogr.*).

In the lower parts of the boundary layers, salinity and velocity gradients are much stronger than they are in the upper parts as these properties transition from their near-surface values to their values in the quiescent deep water of the simulation. Downwind velocity in case S is again an exception, as the shear is similar throughout the boundary layer. The distinctions between the upper and lower parts of the surface boundary layer lead us to label them as the mixed layer and halocline, respectively, but we note that the mixed layer is not truly homogeneous. The transition between the halocline and the mixed layer is generally more abrupt in cases SW and W than in case S. In cases S and SW, the halocline thickness and stratification vary with inertial oscillations. The halocline

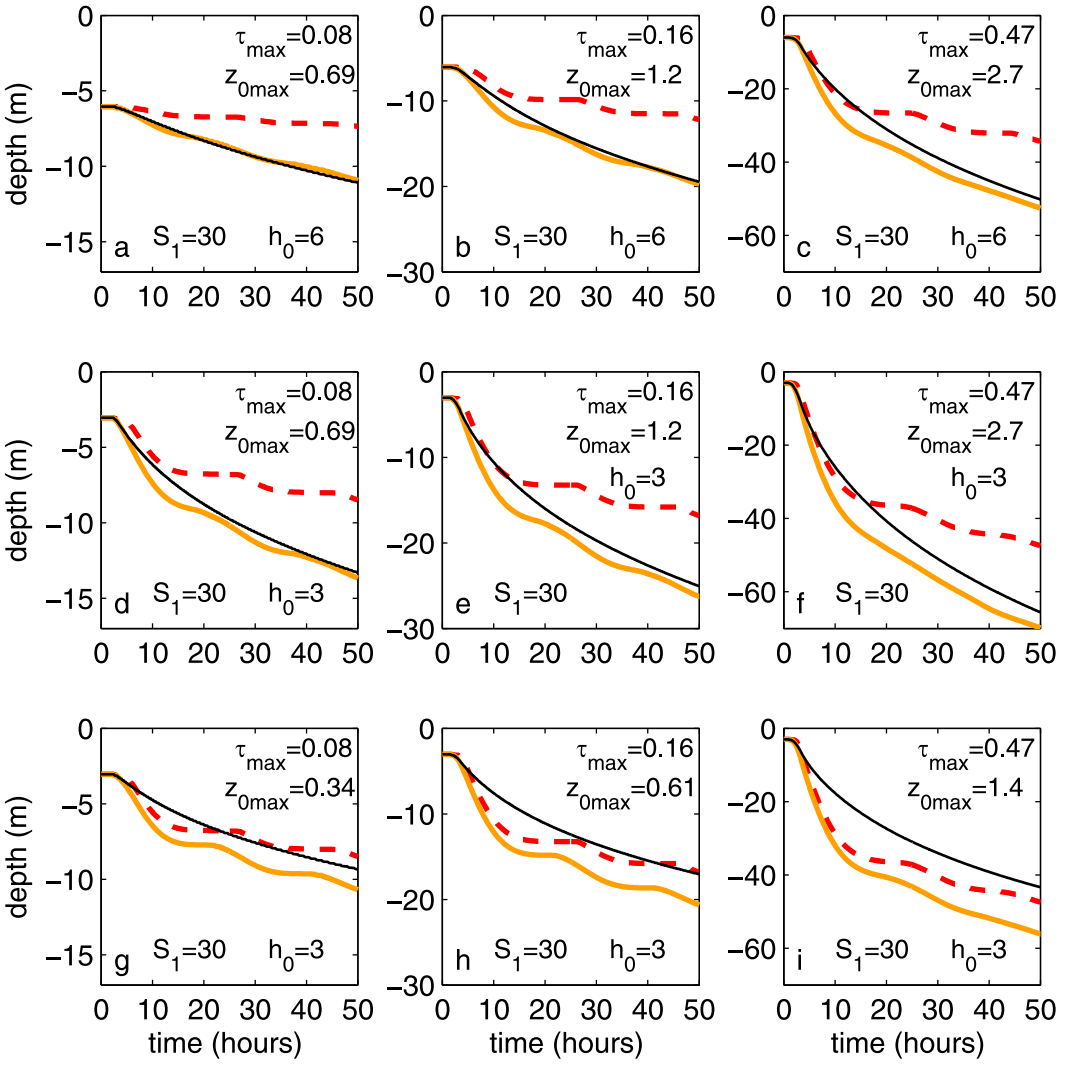

FIG. 5. Evolution of boundary layer thickness for different forcing and initial conditions. Lines show thickness in cases S, SW, and W with same line styles as in Fig. 2. All simulations have initial upper-layer salinity of 30. Wind stress and wave height change from left to right. Initial boundary layer thickness changes from top to middle panels. Surface mixing length changes from middle to bottom panels. Top and middle rows use $z_0 = 0.5H_s$, and bottom row uses $z_0 = 0.25H_s$. Inset text gives maximum wind stress (Pa), maximum mixing length (m), initial boundary layer thickness (m), and initial upper-layer salinity for each set of simulations. (b),(e) The same simulations as in Figs. 4b and 4e. (e) shows the reference simulations, which are also shown in Fig. 3. Note the different y-axis scales.

fills about ¼ to ⅓ of the boundary layer during rapid thickening (e.g., hour 8) and becomes thinner and more strongly stratified during slow-thickening periods (e.g., hour 20). In case W, the halocline is thin and strongly stratified at all times. The boundary layer structures of cases SW and W are very similar during the slow-thickening phases of case SW.

c. *Boundary layer TKE*

Here, we examine the terms in the TKE budget in the boundary layer after spinup. We focus on cases S and SW because the dynamics of case W show little variation in time. TKE dynamics in simulations with and without rotation are similar in the first 10 h except that the halocline tends be slightly thicker in nonrotating cases.

In case S, the dominant terms in the TKE budget after spinup are dissipation and shear production (Fig. 7). The flux divergence of TKE is negligible in these simulations without whitecapping. The shear production is slightly larger than the dissipation rate at most depths, and this mismatch is accounted for by the negative buoyancy production associated with lifting dense, salty water as

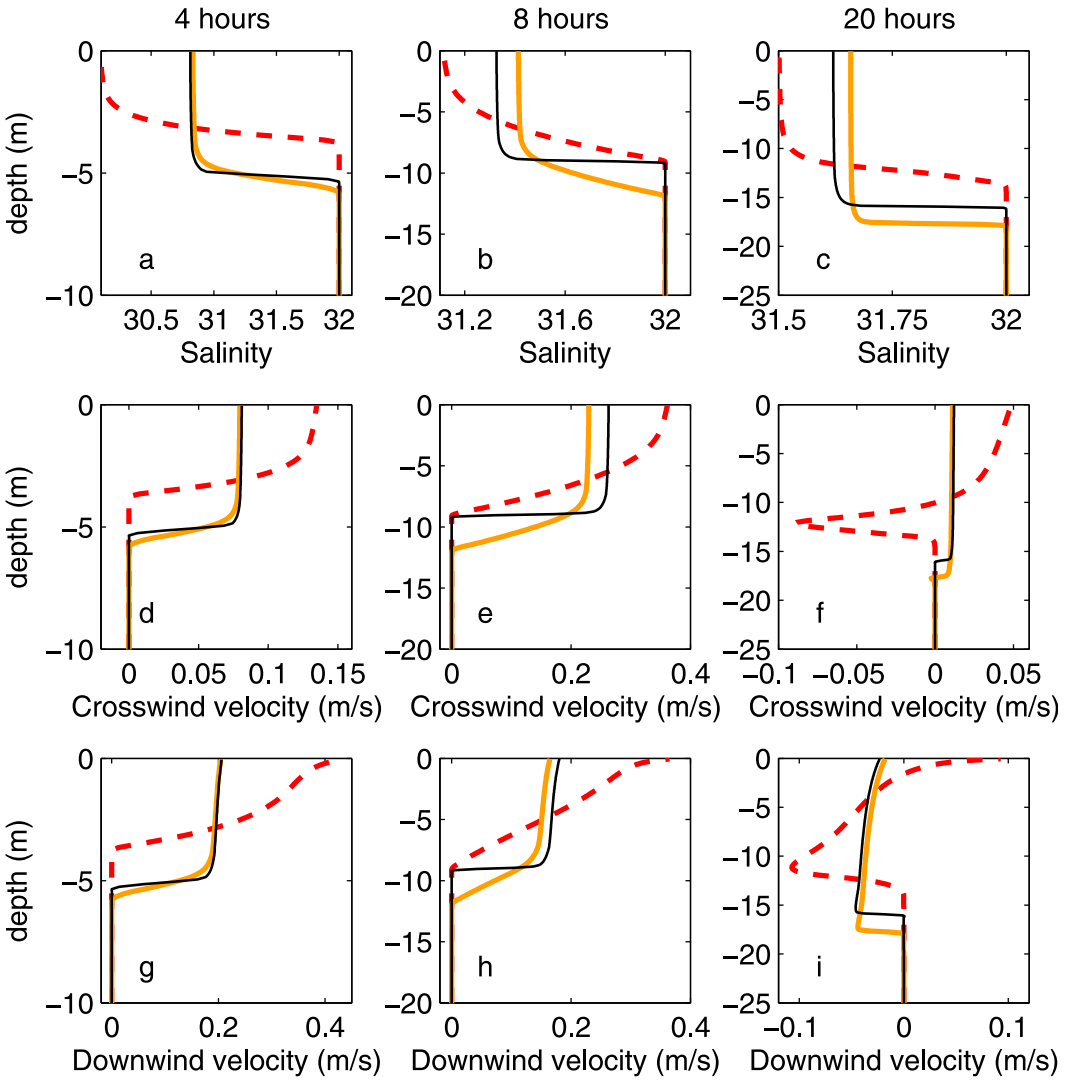

FIG. 6. Profiles of salinity and velocity after 4, 8, and 20 h of simulation in cases with rotation and reference values of forcing and initial conditions (maximum $\tau = 0.16$ Pa, maximum $z_0 = 1.2$ m, $h_0 = 3$ m, and $S_1 = 30$). Line styles are the same as in Fig. 2. Values are means over 15 min. (a)–(c) Salinity. (d)–(f) Crosswind velocity. (g)–(i) Downwind velocity. Note the different x and y axis scales in different panels.

the boundary layer thickens. As the thickening rate varies, the magnitudes and vertical structures of all the terms in the TKE budget vary, but shear production and dissipation remain the dominant terms.

In case SW, the dominant terms vary in both time and space within the boundary layer. In the weakly stratified mixed layer, the dominant TKE balance is between dissipation and flux divergence. Shear production and buoyancy production are small. When the halocline is well developed, flux divergence in the halocline is negligible, and a balance of shear production and dissipation is dominant, again with a small part related to buoyancy production. At these times, the TKE balance in the halocline is similar in both cases S and SW. The TKE that has been transported downward from the surface either has been used for mixing in the upper halocline or it has dissipated at the top of the halocline. During phases of inertial oscillations when shear production is reduced and the halocline in case SW is thin (around 18–20 h), shear production in case SW is weak and flux divergence is important throughout the full thickness of the boundary layer. When shear production at the base of the boundary layer increases (around 25–30 h), the halocline redevelops and the thickening rate increases. During these later thickening events the halocline occupies a reduced fraction of the boundary layer,

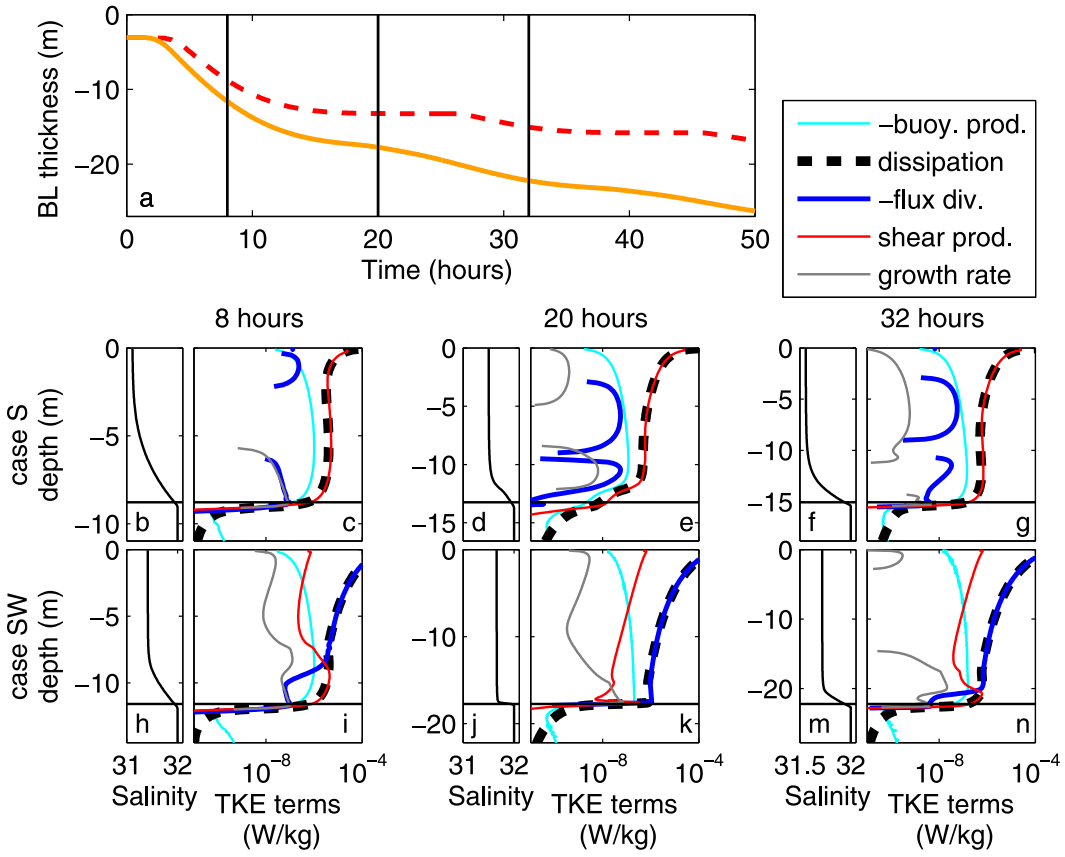

FIG. 7. Boundary layer thickness evolution and vertical profiles of salinity and terms in the TKE budget for simulations in reference conditions. (a) Boundary layer thickness in cases S and SW (symbols are as in Fig. 2). (b),(d),(f) Salinity in case S at times 8, 20, and 32 h. (h),(j),(m) Salinity in case SW at times 8, 20, and 32 h. (c),(e),(g) Terms in TKE budget for case S at times 8, 20, and 32 h. (i),(k),(n) Terms in TKE budget for case SW at times 8, 20, and 32 h. The vertical lines indicate times shown in (b)–(n). Values for TKE terms are means over 15 min. Horizontal lines in (b)–(n) show the base of the boundary layer. Legend explains line styles for (c),(e),(g),(i),(k), and (n). Note variation in *y* axis scales.

and it takes a few hours of rapid thickening for shear production to become well developed.

4. Discussion

Three important observations stand out: 1) In simulations with whitecapping the boundary layer begins to thicken earlier than it does in simulations without whitecapping. 2) Both shear production and whitecapping are important energy sources for increasing the gravitational potential energy of the water column. 3) The dynamics of boundary layer thickening are strongly affected by rotation.

a. Onset of thickening

The effects of whitecapping on thickness are related to the ability of whitecapping-related processes to bring energy and momentum to the base of the boundary layer. As shown during inertial oscillations, whitecapping TKE can be transported to the boundary layer base and be used for mixing at times when shear production is weak. This also occurs at the onset of thickening in the first few hours of the simulation (Figs. 8, 9). The timing of the initiation of thickening could be particularly important in areas with variable winds, so we examine this in some detail. We refer to simulations with rotation, but over these short time periods the results are nearly identical for simulations without rotation.

For this discussion, we define meaningful thickening as times when the thickening rate is faster than 20% of the maximum thickening rate in a given simulation. Other definitions (e.g., a different rate threshold or using an absolute change in boundary layer thickness) lead to similar qualitative interpretations as those made here. The timings and best definition of ''meaningful'' are slightly different for simulations with different forcing

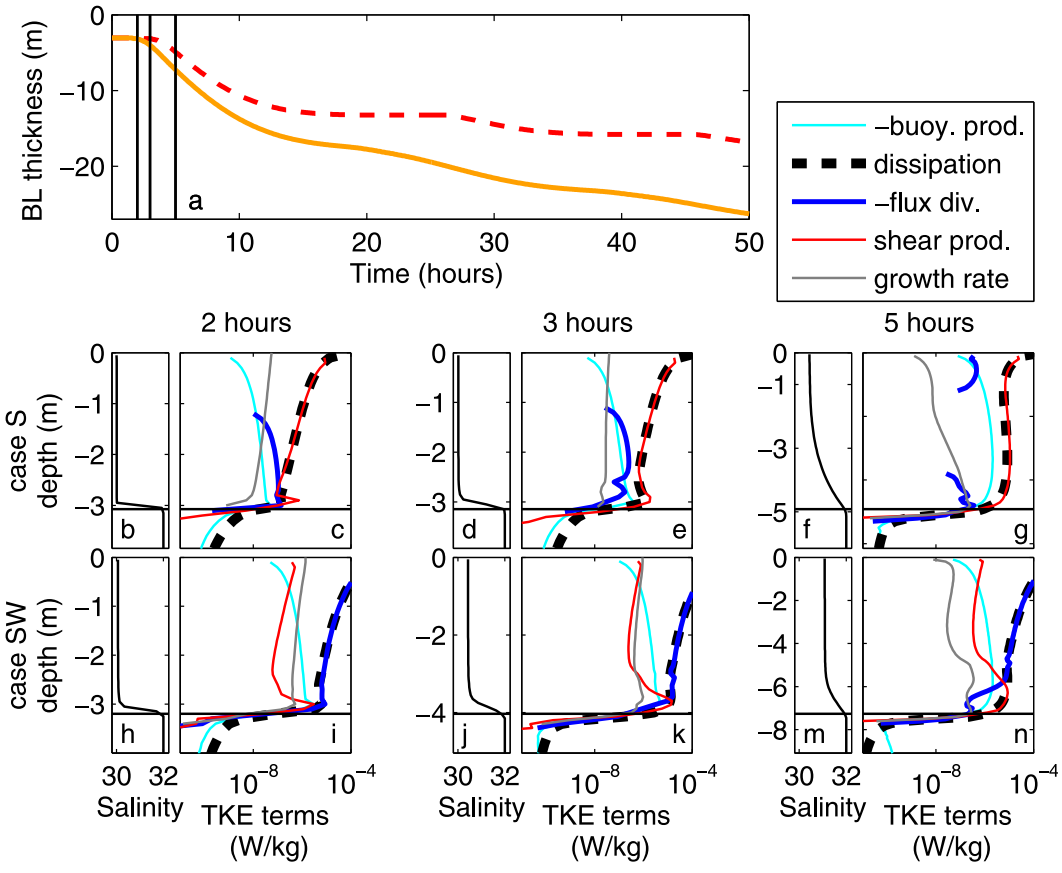

FIG. 8. As in Fig. 7, but at times 2, 3, and 5 h.

and initial conditions, but the general behavior is consistent across conditions. We quantify the energetics by averaging the source terms across the lowest 0.5 m of the boundary layer.

Meaningful thickening of the boundary layer first occurs at roughly the same time for cases SW and W, roughly an hour earlier than for case S for the reference forcing and initial conditions (Fig. 9a). Under strong wind stress, all simulations thicken sooner and the time difference between thickening of cases SW and S is reduced. At the start of thickening in case SW, the average flux divergence of TKE is larger than the average shear production in the lowest 0.5 m of the boundary layer by one to two orders of magnitude (Figs. 8i, 9c,d). The shear production in the first few hours is similar in cases S and SW (although it is consistently larger in case SW). In case W, there is no shear production, but the flux divergence and the time of the start of thickening are similar to those in case SW. These observations suggest that the downward transport of TKE from the sea surface is the primary energy source for initiating thickening in the cases with whitecapping. In contrast, in case S the flux divergence at the boundary layer base is always smaller than the shear production, and shear production is the primary energy source for initiating thickening. In cases SW and W, order of magnitude estimates (not shown) suggest that the timing of the onset of thickening is likely related to the diffusion time scale for transport of TKE from the surface to the base of the boundary layer. In case S, examination of the velocity field (Fig. 9e) suggests that the timing of the onset of thickening is likely related to the time required for the mean velocities to develop enough to allow substantial shear production at the base of the boundary layer.

About an hour after thickening starts, flux of TKE to the base of the boundary layer in case SW decreases and eventually becomes similar to the value in case S. TKE is still being injected at the sea surface, but at these times the TKE transport is reduced higher up in the halocline and does not reach the boundary layer base. After about 3 h in case SW, more energy is introduced to the base of the boundary layer by shear production than by TKE flux. After about 4 h, the energy input by each of shear production and TKE flux is similar in cases S and SW. This coincides with cases S and SW having similar thickening rates and is consistent with the suggestion

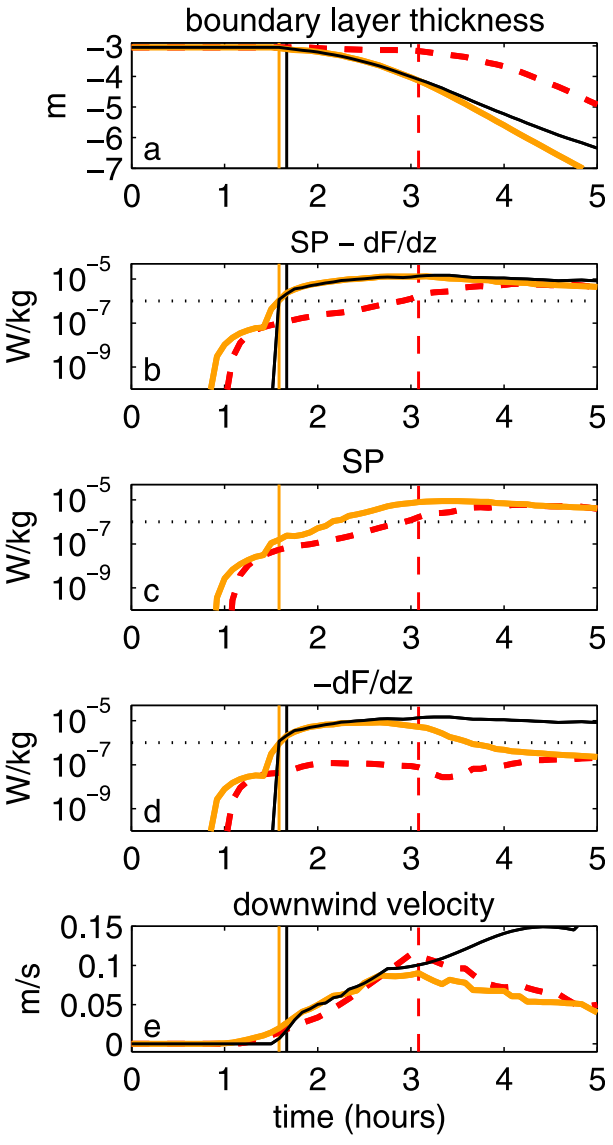

FIG. 9. Evolution of boundary layer thickness and turbulence quantities during the early hours of the wind event for simulations with reference conditions. Turbulence quantities and downwind velocity are means over grid cells between 0 and 0.5 m above the 31.94-psu isohaline. (a) Boundary layer thickness. (b) Sum of shear production and magnitude of flux divergence of TKE ($-dF/dz$). (c) Shear production. (d) Magnitude of flux divergence of TKE. (e) Downwind velocity. Line styles represent the same simulations as in Fig. 2. All results are smoothed with a 15-min boxcar filter. The filter length is truncated at the start of each record. Dashed lines in (b),(c), and (d) at 10^{-6} W kg^{-1} are shown for visual reference and have no general physical significance. The simulations shown in this figure were made in the rotating reference frame (cases S, SW, and W), but nonrotating simulations show almost no difference from these quantities over this time period.

that in both cases shear production is the primary energy source for thickening after the velocity field in the upper layer is well developed. These dynamics are similar under a range of forcing and initial conditions, although in simulations with stronger winds, thickening begins earlier than in simulations with weaker winds.

b. *Energy source for thickening*

Similarly to the numerical results found above, analytical models also predict that after spinup but before significant effects of inertial oscillations, shear production is the primary energy source for thickening under most of the forcing and initial conditions studied here. To examine the relative importance of transport and shear production in providing TKE for buoyancy flux after spinup, we compare two analytical models for a two-layer system in which the upper layer is deepening into the lower layer. The upper layer has density ρ_1 that is uniform in z but increases with time, and the lower layer has constant uniform density ρ_2. The first model was developed by Trowbridge (1992) and uses shear production as the source of TKE. We develop the second model using the whitecapping model of Burchard (2001).

Trowbridge determined a thickening rate due to shear production by assuming a critical gradient Richardson number [his (15)]:

$$\frac{dh}{dt} = \frac{3}{2}\frac{\mathrm{Ri}_c^{1/2} u_*^2}{B^{1/2}}, \tag{14}$$

where h is the thickness of the upper layer (equivalent to base of the halocline in these simulations), t is the time, and Ri_c is a critical gradient Richardson number, taken to be 0.25. Because the vertically integrated buoyancy anomaly is constant in time, the thickening rate in (14) is also constant when the wind stress has reached its steady value in this model.

Burchard (2001), building on work by Craig (1996), developed an analytical solution for the steady-state vertical structure of TKE and dissipation rate under whitecapping in the absence of shear production in unstratified water. As in the ROMS simulations, whitecapping is approximated in the analytical model as a TKE flux through the sea surface. Burchard (2001) approximates F_0 as proportional to $-u_*^3$, but the precise form of F_0 does not need to be specified in the development of the following relationships. We continue to use (2) in the development of our predictions for dh/dt due to whitecapping. Burchard predicts the vertical structure of the dissipation rate deeper than one mixing length below the mean sea surface [his (13)] to be

$$\varepsilon = -F_b m |z_b|^m |z|^{-(m+1)}, \tag{15}$$

where $m \approx 1.677$ is a constant derived from coefficients in the k–ε model (Burchard 2001); $z_b = -z_0$ is a negative value, one mixing length below the sea surface (approximately the level of the wave troughs); and $F_b = F(z_b)$ is the flux of TKE downward past z_b. Although we lack a complete understanding of dissipation rates above trough level (Gemmrich 2010), we determine

$$F_b = \frac{F_0}{m+1} \tag{16}$$

by assuming uniform dissipation rates above trough level (Terray et al. 1996; Burchard 2001).

In this unstratified model, the TKE transported downward past any depth $F(z)$ is the amount of TKE injected by whitecapping that is not dissipated at depths above z and can be computed by integrating (15):

$$F(z) = F_b - \int_z^{z_b} dz\varepsilon = F_b\left(\frac{z}{z_b}\right)^{-m}. \tag{17}$$

We adapted Burchard's model for this study by assuming that the TKE and dissipation profiles in the surface boundary layer are the same as his prediction at depths above $z = -h$ and that the TKE that is transported through $z = -h$ is used to increase the gravitational potential energy by mixing dense fluid upward as the boundary layer thickens. This model ignores the decrease in turbulent length scales that are caused by the stratification in the halocline (Scully et al. 2011) or, equivalently, the base of the upper layer in the two-layer model. These would increase the dissipation rate [as observed in shallow water by Feddersen et al. (2007)] and decrease the turbulent diffusivity at the base of the surface boundary layer of the simulations, causing decreased transport of TKE to the base of the boundary layer.

The gravitational potential energy per unit of horizontal area normalized by the density of the lower layer is

$$E = \frac{1}{\rho_2}\int_{-H}^{0} dz\,\rho g(z+H), \tag{18}$$

where the $z + H$ gives the distance above the bottom. As the upper layer thickens, E increases at a rate

$$\frac{dE}{dt} = \frac{B}{2}\frac{dh}{dt}. \tag{19}$$

Assuming that the TKE transported from whitecapping does the work to increase E, we equate the magnitude of (17) with (19) at $z = -h$ to find the rate of thickening of the upper layer as

$$\frac{dh}{dt} = -\frac{2F_b}{B}\left(\frac{h}{|z_b|}\right)^{-m}. \tag{20}$$

The magnitude of (17) is used because the downward flux is negative, but it acts as a source of gravitational potential energy for mixing. This analysis gives some insight into why the effect of reducing z_0 is larger than the effect of reducing c_e in our simulations. The thickening rate is proportional to c_e through F_b, but it is proportional to z_0^m. Because m is larger than 1, (20) implies that changing the surface roughness length will have a larger effect than changing c_e by the same relative amount.

Comparing (14) and (20), we find that the boundary layer thickness at which these thickening rates are equal is

$$h_{\mathrm{eq}} = -z_b\left[\frac{4}{3}\frac{-F_b}{u_*^2}\left(\frac{1}{\mathrm{Ri}_c B}\right)^{1/2}\right]^{1/m}. \tag{21}$$

This result depends on the parameters describing the energy transfer from the waves to turbulence and from the mean flow to turbulence (F_b and Ri_c, respectively). For thin boundary layers, where $h < h_{\mathrm{eq}}$, the thickening rate due to whitecapping exceeds the thickening rate due to shear instability, and for thick boundary layers, where $h > h_{\mathrm{eq}}$, the thickening rate due to shear instability exceeds the thickening rate due to whitecapping. This is equivalent to finding that for thin boundary layers the dominant source of energy for thickening is likely to be whitecapping, and for thick boundary layers, the dominant source of energy for thickening is likely to be shear instability.

The thickening rate due to shear instability is proportional to u_*^2 [(14)]. However, because c_e increases with wind speed, F_b increases at a faster than linear rate with u_*^2 (using 16, 2, 3, and 4), and stronger wind stresses will lead to thicker whitecapping-dominated layers (Fig. 10). Similarly, large integrated buoyancy anomalies will lead to thinner whitecapping-dominated layers. The value of h_{eq} depends linearly on the turbulent mixing length for whitecapping z_0. Because z_0 is related to the significant height of the wind waves (Terray et al. 1996; Gerbi et al. 2009) and because wind waves may evolve much more slowly than the wind stress, the relative importance of shear production and whitecapping will depend on the wave age. For the range of conditions in this study after the waves are fully developed, h_{eq} varies between ~20 (large τ, small B) and ~2 m (small τ, large B). In the first several hours of a wind event or in fetch-limited conditions, smaller wave heights and consequently smaller z_0 will limit h_{eq} to smaller values and

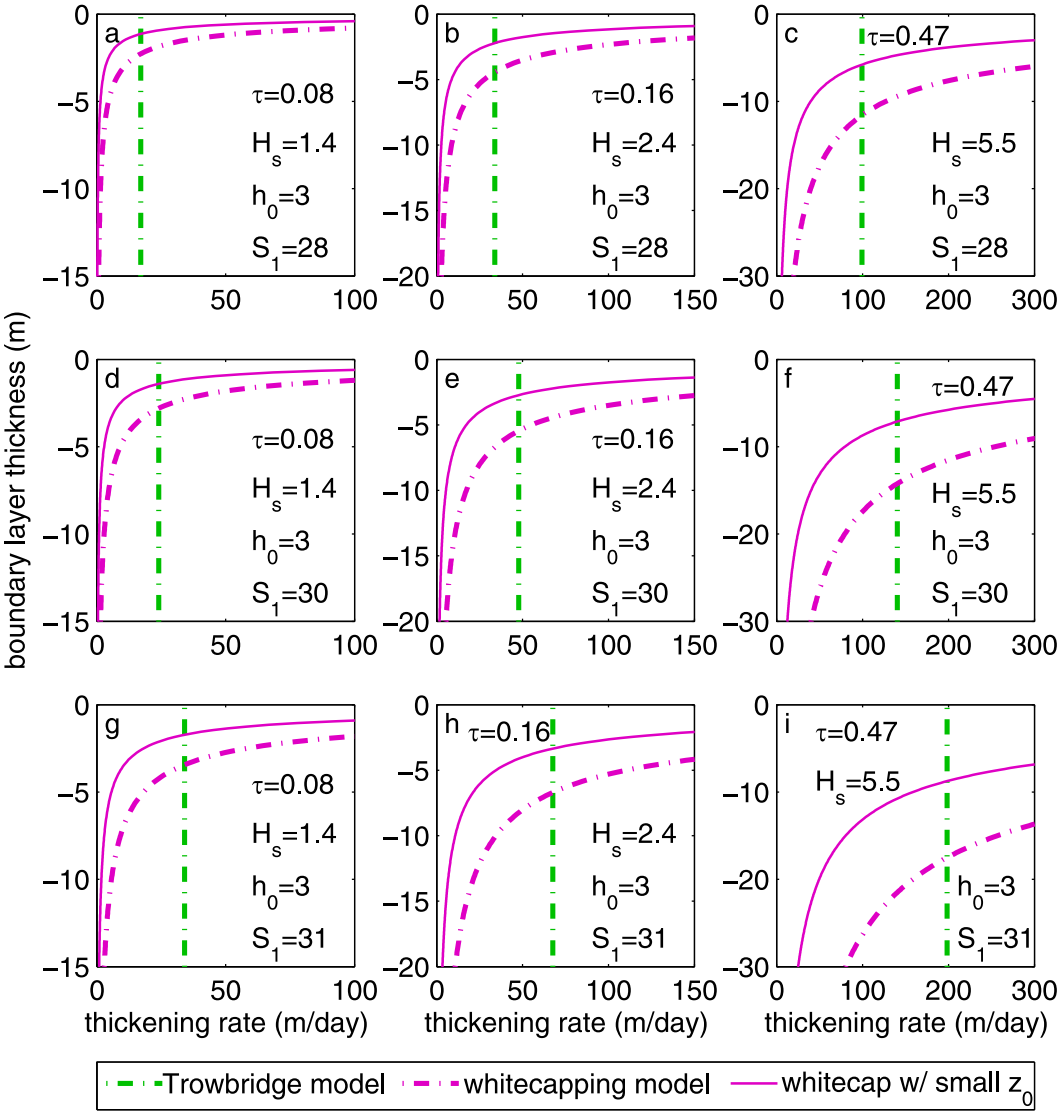

FIG. 10. Theoretical predictions of thickening rates under steady forcing using (14) and (20) and a range of initial and forcing conditions. The Trowbridge model (vertical lines) predicts a constant thickening rate for two-layer initial conditions. We evaluated the whitecapping model using $z_0 = 0.5H_s$ (dashed–dotted lines) and $z_0 = 0.25H_s$ (thin solid lines). Inset text gives the maximum wind stress (Pa), significant wave height (m), initial boundary layer thickness (m), and initial upper-layer salinity for each set of simulations.

will reduce the effect of whitecapping in thickening the boundary layer.

Analytical predictions of upper-layer thickness can be determined using either (14) or (20) and integrating in time

$$h(t) = h_0 + \int_0^t dt' \frac{dh}{dt'}, \tag{22}$$

where t' is an integration variable representing time. We performed these integrations using the instantaneous values of wind stress and significant wave height. This assumes an equilibrium between the turbulence and the wind that is almost certainly not valid in the first hours of simulation. One consequence of this assumption is that the boundary layer predicted using (14) begins thickening before the boundary layer in the simulations.

In case W, the thickness of the surface boundary layer is similar to but slightly larger than the analytical prediction determined using (20) (Fig. 11). This direction of offset is opposite what is expected by ignoring the stratification effects in the analytical model and is likely caused by other simplifications made in developing (20). In case S, the boundary layer thickness increases at a

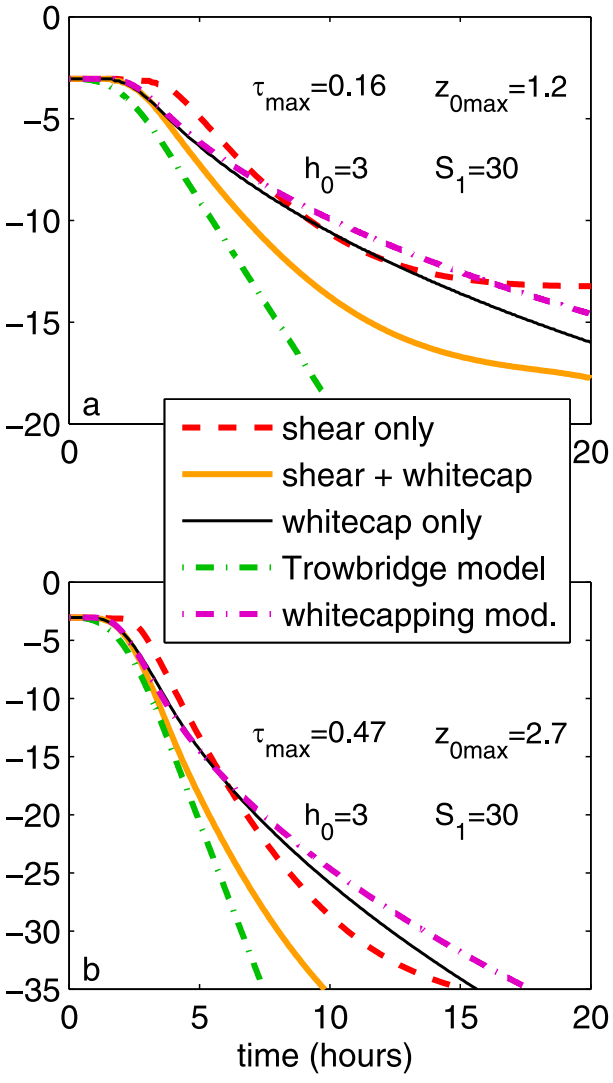

FIG. 11. Evolution of boundary layer thickness from simulations and theoretical predictions using (14), (20), and (22). (a) Reference values of forcing and initial conditions. (b) Initial conditions as in (a), but larger wind stress and surface mixing length. Thickening rates used in integration of analytical predictions were determined using the time-dependent values of wind stress and wave height shown in Fig. 1. Inset text gives maximum wind stress (Pa), maximum mixing length (m), initial boundary layer thickness (m), and initial upper-layer salinity for each set of simulations.

rate similar to but slightly smaller than that predicted by the shear production model [(14)] until about hour 10 (Fig. 11). As might be expected from the dominance of shear production in the turbulence energetics after spinup, the boundary layer in case SW also thickens at a rate similar to the shear production prediction [(14)] before inertial oscillations reduce the thickening rate. We note that the thickening rates for cases S and W are more similar than predicted by the analytical models in (14) and (20), so the dominance of shear production over whitecapping is not as pronounced in the simulations as the analytical models would suggest. Results from nonrotating simulations show constant thickening rates (Fig. 2) that are smaller than but within 25% of the Trowbridge prediction for most of the conditions in this study.

c. *Relationship to Langmuir turbulence*

Wind-forced waves and whitecapping are often but not always accompanied by Langmuir turbulence (e.g., Smith 1992), whose effects were not included in these simulations. Langmuir turbulence extracts energy from the waves via Stokes drift shear (Stokes production; McWilliams et al. 1997; Teixeira and Belcher 2002), and it also forms coherent structures that lead to increased turbulent viscosity and diffusivity for a given TKE (Gemmrich and Farmer 1999; Sullivan et al. 2007). The energy input from Stokes production is concentrated near the surface where Stokes shear is strongest, and the vertically integrated energy input from Stokes production is no larger than $u_s u_*^2$, where u_s is the surface Stokes drift (assuming that the stress magnitude decreases with depth; McWilliams et al. 1997; Teixeira and Belcher 2002). Because Stokes drift is small compared to the whitecapping energy transfer velocity c_e, the total energy input by Stokes production is small compared to that of whitecapping.

Observations have shown that Langmuir turbulence enhances turbulent diffusivity of heat near the surface (Gemmrich and Farmer 1999) and that the downwelling limbs of Langmuir cells concentrate water with high dissipation rates and transport it downward (Thorpe et al. 2003). More recent observations (Scully et al. 2015, manuscript submitted to *J. Phys. Oceanogr.*) show that under whitecapping conditions, vertical TKE transport is stronger when Langmuir turbulence is present. In the context of the study presented here, if Langmuir turbulence is able to increase the turbulent diffusivity, it will help deliver more TKE from the sea surface to the halocline and increase the ability of whitecapping to thicken the boundary layer. However, other studies have hypothesized or shown that Langmuir turbulence can concentrate bubble clouds enough to suppress turbulence and organized Langmuir structures, at least very near the surface (Smith 1998; Gemmrich 2012). In those conditions, Langmuir turbulence is unlikely to enhance the transport of TKE to the base of the boundary layer for mixing, and by concentrating high TKE water and bubbles, Langmuir turbulence could, conceivably, reduce the amount of TKE available for boundary layer mixing.

Large-eddy simulations by Kukulka et al. (2010) have shown that Langmuir turbulence can enhance the rate of

rapid boundary layer thickening without wave breaking. The chief mechanism identified in that study was Langmuir structures enhancing Eulerian shear and shear production at the base of the boundary layer. Our results have shown that when shear production is strong, it is the dominant energy source for mixing, but when it is weak, TKE from whitecapping will also thicken the boundary layer. Combining the observations of Scully et al. (2015, manuscript submitted to *J. Phys. Oceanogr.*) and the simulations of Kukulka et al. (2010) with our results suggests that whitecapping and Langmuir turbulence can work together to enhance surface boundary layer thickening, at least under conditions when bubble convergence does not reduce whitecapping TKE significantly.

5. Conclusions

We conducted numerical experiments on turbulence dynamics and the thickening of the ocean surface boundary layer. We sought to determine the relative importance of whitecapping surface waves and shear production as sources of the turbulent kinetic energy that is responsible for vertical buoyancy flux at the base of the boundary layer across a range of forcing and initial conditions.

We found that initial boundary layer thickening occurs earlier in simulations that include a whitecapping parameterization than in simulations that do not. This is caused by the transport of whitecapping TKE to the base of the boundary layer. Within several hours of the start of a wind event, however, whitecapping is not the dominant source of TKE for thickening the boundary layer. Shear production in the halocline is a much stronger energy source. This is confirmed both in the numerical results and by examining analytical models of shear-induced thickening (Trowbridge 1992) and whitecapping-induced thickening (Burchard 2001 and developed here).

In simulations without rotation, thickening by shear production proceeds at a constant rate in simulations with and without whitecapping. In simulations with rotation, the rate of thickening varies with the phase of inertial oscillations, and thickening rates are periodically near zero in simulations without whitecapping. In simulations that have both whitecapping and shear production, the reduction of the thickening rate by inertial oscillations is minimized and the mean thickening rate is faster than it is in simulations with only shear production. This is largely due to the vertical flux of TKE supplying energy to the boundary layer base when shear production is weak.

These results are somewhat sensitive to the choice of uncertain parameters that represent difficult to quantify physical processes: surface mixing length and surface TKE flux under whitecapping surface waves. Reducing these parameters within a reasonable range reduces but does not eliminate the effects of whitecapping on surface boundary layer thickening.

Acknowledgments. We thank Skidmore College for financial and infrastructure support, and Skidmore and the National Science Foundation for funding travel to meetings where early versions of this work were presented. We also thank the National Science Foundation, Oregon State University, Jonathan Nash, and Joe Jurisa for funding and hosting a workshop on River Plume Mixing in October, 2013, where ideas and context for this paper were developed. Last, but not least, we thank Jim Thomson, Jerry Smith, and one anonymous reviewer for comments that strengthened the manuscript.

REFERENCES

Agrawal, Y. C., E. A. Terray, M. A. Donelan, P. A. Hwang, A. J. Williams III, W. M. Drennan, K. K. Kahma, and S. A. Kitaigorodskii, 1992: Enhanced dissipation of kinetic energy beneath surface waves. *Nature,* **359,** 219–220, doi:10.1038/359219a0.

Breugem, W. A., and L. H. Holthuijsen, 2007: Generalized shallow water wave growth from Lake George. *J. Waterw. Port Coastal Ocean Eng.,* **133,** 173–182, doi:10.1061/(ASCE)0733-950X(2007)133:3(173).

Burchard, H., 2001: Simulating the wave-enhanced layer under breaking surface waves with two-equation turbulence models. *J. Phys. Oceanogr.,* **31,** 3133–3145, doi:10.1175/1520-0485(2001)031<3133:STWELU>2.0.CO;2.

——, and H. Baumert, 1995: On the performance of a mixed-layer model based on the *k*-ε turbulence closure. *J. Geophys. Res.,* **100,** 8523–8540, doi:10.1029/94JC03229.

Carniel, S., J. C. Warner, J. Chiggiato, and M. Sclavo, 2009: Investigating the impact of surface wave breaking on modeling the trajectories of drifters in the northern Adriatic Sea during a wind-storm event. *Ocean Modell.,* **30,** 225–239, doi:10.1016/j.ocemod.2009.07.001.

Craig, P. D., 1996: Velocity profiles and surface roughness under breaking waves. *J. Geophys. Res.,* **101,** 1265–1277, doi:10.1029/95JC03220.

——, and M. L. Banner, 1994: Modeling wave enhanced turbulence in the ocean surface layer. *J. Phys. Oceanogr.,* **24,** 2546–2559, doi:10.1175/1520-0485(1994)024<2546:MWETIT>2.0.CO;2.

Craik, A. D. D., and S. Leibovich, 1976: A rational model for Langmuir circulations. *J. Fluid Mech.,* **73,** 401–426, doi:10.1017/S0022112076001420.

D'Asaro, E. A., 2014: Turbulence in the upper-ocean mixed layer. *Annu. Rev. Mar. Sci.,* **6,** 101–115, doi:10.1146/annurev-marine-010213-135138.

——, J. Thomson, A. Y. Shcherbina, R. R. Harcourt, M. F. Cronin, M. A. Hemer, and B. Fox-Kemper, 2014: Quantifying upper ocean turbulence driven by surface waves. *Geophys. Res. Lett.,* **41,** 102–107, doi:10.1002/2013GL058193.

Drennan, W. M., M. A. Donelan, E. A. Terray, and K. B. Katsaros, 1996: Oceanic turbulence dissipation measurements in

SWADE. *J. Phys. Oceanogr.,* **26,** 808–815, doi:10.1175/1520-0485(1996)026<0808:OTDMIS>2.0.CO;2.

Fairall, C., E. Bradley, J. Hare, A. Grachev, and J. Edson, 2003: Bulk parameterizations of air–sea fluxes: Updates and verification for the COARE algorithm. *J. Climate,* **16,** 571–591, doi:10.1175/1520-0442(2003)016<0571:BPOASF>2.0.CO;2.

Feddersen, F., J. H. Trowbridge, and A. J. Williams III, 2007: Vertical structure of dissipation in the nearshore. *J. Phys. Oceanogr.,* **37,** 1764–1777, doi:10.1175/JPO3098.1.

Gemmrich, J., 2010: Strong turbulence in the wave crest region. *J. Phys. Oceanogr.,* **40,** 583–595, doi:10.1175/2009JPO4179.1.

——, 2012: Bubble-induced turbulence suppression in Langmuir circulation. *Geophys. Res. Lett.,* **39,** L10604, doi:10.1029/2012GL051691.

——, and D. M. Farmer, 1999: Near-surface turbulence and thermal structure in a wind-driven sea. *J. Phys. Oceanogr.,* **29,** 480–499, doi:10.1175/1520-0485(1999)029<0480:NSTATS>2.0.CO;2.

——, T. D. Mudge, and V. D. Polonichko, 1994: On the energy input from wind to surface waves. *J. Phys. Oceanogr.,* **24,** 2413–2417, doi:10.1175/1520-0485(1994)024<2413:OTEIFW>2.0.CO;2.

Gerbi, G. P., J. H. Trowbridge, J. B. Edson, A. J. Plueddemann, E. A. Terray, and J. J. Fredericks, 2008: Measurements of momentum and heat transfer across the air–sea interface. *J. Phys. Oceanogr.,* **38,** 1054–1072, doi:10.1175/2007JPO3739.1.

——, ——, E. A. Terray, A. J. Plueddemann, and T. Kukulka, 2009: Observations of turbulence in the ocean surface boundary layer: Energetics and transport. *J. Phys. Oceanogr.,* **39,** 1077–1096, doi:10.1175/2008JPO4044.1.

——, R. J. Chant, and J. L. Wilkin, 2013: Breaking surface wave effects on river plume dynamics during upwelling-favorable winds. *J. Phys. Oceanogr.,* **43,** 1959–1980, doi:10.1175/JPO-D-12-0185.1.

Haidvogel, D. B., and Coauthors, 2008: Ocean forecasting in terrain-following coordinates: Formulation and skill assessment of the Regional Ocean Modeling System. *J. Comput. Phys.,* **227,** 3595–3624, doi:10.1016/j.jcp.2007.06.016.

Harcourt, R. R., 2015: An improved second-moment closure model of Langmuir turbulence. *J. Phys. Oceanogr.,* **45,** 84–103, doi:10.1175/JPO-D-14-0046.1.

Holthuijsen, L. H., 2007: *Waves in Oceanic and Coastal Waters.* Cambridge University Press, 387 pp.

Hwang, P. A., 2009: Estimating the effective energy transfer velocity at air-sea interface. *J. Geophys. Res.,* **114,** C11011, doi:10.1029/2009JC005497.

Jones, N. L., and S. G. Monismith, 2008a: The influence of whitecapping waves on the vertical structure of turbulence in a shallow estuarine environment. *J. Phys. Oceanogr.,* **38,** 1563–1580, doi:10.1175/2007JPO3766.1.

——, and ——, 2008b: Modeling the influence of wave-enhanced turbulence in a shallow tide- and wind-driven water column. *J. Geophys. Res.,* **113,** C03009, doi:10.1029/2007JC004246.

Jones, W. P., and B. E. Launder, 1972: The prediction of laminarization with a two-equation model of turbulence. *Int. J. Heat Mass Transfer,* **15,** 301–314, doi:10.1016/0017-9310(72)90076-2.

Kukulka, T., A. J. Plueddemann, J. H. Trowbridge, and P. P. Sullivan, 2010: Rapid mixed layer deepening by the combination of Langmuir and shear instabilities: A case study. *J. Phys. Oceanogr.,* **40,** 2381–2400, doi:10.1175/2010JPO4403.1.

——, ——, and P. P. Sullivan, 2012: Nonlocal transport due to Langmuir circulation in a coastal ocean. *J. Geophys. Res.,* **117,** C12007, doi:10.1029/2012JC008340.

McWilliams, J. C., P. P. Sullivan, and C.-H. Moeng, 1997: Langmuir turbulence in the ocean. *J. Fluid Mech.,* **334,** 1–30, doi:10.1017/S0022112096004375.

——, E. Huckle, J.-H. Liang, and P. P. Sullivan, 2012: The wavy Ekman layer: Langmuir circulations, breaking waves, and Reynolds stress. *J. Phys. Oceanogr.,* **42,** 1793–1816, doi:10.1175/JPO-D-12-07.1.

——, ——, ——, and ——, 2014: Langmuir turbulence in swell. *J. Phys. Oceanogr.,* **44,** 870–890, doi:10.1175/JPO-D-13-0122.1.

Munk, W. H., 1947: A critical wind speed for air-sea boundary processes. *J. Mar. Res.,* **6,** 203–218.

Pierson, W. J., and L. Moskowitz, 1964: A proposed spectral form for fully developed wind seas based on the similarity theory of S. A. Kitaigorodskii. *J. Geophys. Res.,* **69,** 5181–5190, doi:10.1029/JZ069i024p05181.

Price, J. F., R. A. Weller, and R. Pinkel, 1986: Diurnal cycling: Observations and models of the upper ocean response to diurnal heating, cooling, and wind mixing. *J. Geophys. Res.,* **91,** 8411–8427, doi:10.1029/JC091iC07p08411.

Scully, M. E., W. R. Geyer, and J. H. Trowbridge, 2011: The influence of stratification and nonlocal turbulent production on estuarine turbulence: An assessment of turbulence closure with field observations. *J. Phys. Oceanogr.,* **41,** 166–185, doi:10.1175/2010JPO4470.1.

Shchepetkin, A. F., and J. C. McWilliams, 2005: The Regional Oceanic Modeling System (ROMS): A split-explicit, free-surface, topography-following-coordinate oceanic model. *Ocean Modell.,* **9,** 347–404, doi:10.1016/j.ocemod.2004.08.002.

——, and ——, 2008: Computational kernel algorithms for fine-scale, multi-process, long-term oceanic simulations. *Computational Methods for the Ocean and the Atmosphere,* P. G. Ciarlet, R. Temam, and J. Tribbia, Eds., Vol. XIV, *Handbook of Numerical Analysis,* Elsevier, 121–183.

——, and ——, 2009: Correction and commentary for "Ocean forecasting in terrain-following coordinates: Formulation and skill assessment of the regional ocean modeling system" by Haidvogel et al., J. Comp. Phys. 227, pp. 3595–3624. *J. Comput. Phys.,* **228,** 8985–9000, doi:10.1016/j.jcp.2009.09.002.

Smith, J. A., 1992: Observed growth of Langmuir circulation. *J. Geophys. Res.,* **97,** 5651–5664, doi:10.1029/91JC03118.

——, 1998: Evolution of Langmuir circulation during a storm. *J. Geophys. Res.,* **103,** 12 649–12 668, doi:10.1029/97JC03611.

Soloviev, A., and R. Lukas, 2003: Observation of wave-enhanced turbulence in the near-surface layer of the ocean during TOGA COARE. *Deep-Sea Res. I,* **50,** 371–395, doi:10.1016/S0967-0637(03)00004-9.

Sullivan, P. P., J. C. McWilliams, and W. K. Melville, 2004: The oceanic boundary layer driven by wave breaking with stochastic variability. Part 1. Direct numerical simulations. *J. Fluid Mech.,* **507,** 143–174, doi:10.1017/S0022112004008882.

——, ——, and ——, 2007: Surface gravity wave effects in the oceanic boundary layer: Large-eddy simulation with vortex force and stochastic breakers. *J. Fluid Mech.,* **593,** 405–452, doi:10.1017/S002211200700897X.

——, L. Romero, J. C. McWilliams, and W. K. Melville, 2012: Transient evolution of Langmuir turbulence in ocean boundary layers driven by hurricane winds and waves. *J. Phys. Oceanogr.,* **42,** 1959–1980, doi:10.1175/JPO-D-12-025.1.

Teixeira, M. A. C., 2012: The influence of Langmuir turbulence on the scaling for the dissipation rate in the oceanic boundary layer. *J. Geophys. Res.,* **117,** C05015, doi:10.1029/2011JC007235.

——, and S. E. Belcher, 2002: On the distortion of turbulence by a progressive surface wave. *J. Fluid Mech.,* **458,** 229–267, doi:10.1017/S0022112002007838.

Terray, E. A., M. A. Donelan, Y. C. Agrawal, W. M. Drennan, K. K. Kahma, A. J. Williams III, P. A. Hwang, and S. A. Kitaigorodskii, 1996: Estimates of kinetic energy dissipation under breaking waves. *J. Phys. Oceanogr.,* **26,** 792–807, doi:10.1175/1520-0485(1996)026<0792:EOKEDU>2.0.CO;2.

Thomson, J., E. A. D'Asaro, M. F. Cronin, W. E. Rogers, R. R. Harcourt, and A. Shcherbina, 2013: Waves and the equilibrium range at Ocean Weather Station P. *J. Geophys. Res. Oceans,* **118,** 5951–5962, doi:10.1002/2013JC008837.

——, A. R. Horner-Devine, S. Zippel, C. Rusch, and W. Geyer, 2014: Wave breaking turbulence at the offshore front of the Columbia River plume. *Geophys. Res. Lett.,* **41,** 8987–8993, doi:10.1002/2014GL062274.

Thorpe, S. A., T. R. Osborn, J. F. E. Jackson, A. J. Hall, and R. G. Lueck, 2003: Measurements of turbulence in the upper-ocean mixing layer using autosub. *J. Phys. Oceanogr.,* **33,** 122–145, doi:10.1175/1520-0485(2003)033<0122:MOTITU>2.0.CO;2.

Trowbridge, J., 1992: A simple description of the deepening and structure of a stably stratified flow driven by a surface stress. *J. Geophys. Res.,* **97,** 15 529–15 543, doi:10.1029/92JC01512.

Vagle, S., J. Gemmrich, and H. Czerski, 2012: Reduced upper ocean turbulence and changes to bubble size distributions during large downward heat flux events. *J. Geophys. Res.,* **117,** C00H16, doi:10.1029/2011JC007308.

Warner, J. C., C. R. Sherwood, H. G. Arango, and R. P. Signell, 2005: Performance of four turbulence closure models implemented using a generic length scale method. *Ocean Modell.,* **8,** 81–113, doi:10.1016/j.ocemod.2003.12.003.

Young, I., and L. Verhagen, 1996: The growth of fetch limited waves in water of finite depth. Part 1. Total energy and peak frequency. *Coastal Eng.,* **29,** 47–78, doi:10.1016/S0378-3839(96)00006-3.

Zhang, X., G. Han, D. Wang, W. Li, and Z. He, 2011: Effect of surface wave breaking on the surface boundary layer of temperature in the Yellow Sea in summer. *Ocean Modell.,* **38,** 267–279, doi:10.1016/j.ocemod.2011.04.006.